ORIGINALS

**Bharathram Ganapathisubramani · Ellen K. Longmire
Ivan Marusic · Stamatios Pothos**

Dual-plane PIV technique to determine the complete velocity gradient tensor in a turbulent boundary layer

Abstract Simultaneous dual-plane PIV experiments, which utilized three cameras to measure velocity components in two differentially separated planes, were performed in streamwise-spanwise planes in the log region of a turbulent boundary layer at a moderate Reynolds number ($Re_\tau \sim 1100$). Stereoscopic data were obtained in one plane with two cameras, and standard PIV data were obtained in the other with a single camera. The scattered light from the two planes was separated onto respective cameras by using orthogonal polarizations. The acquired datasets were used in tandem with continuity to compute all 9 velocity gradients, the complete vorticity vector and other invariant quantities. These derived quantities were employed to analyze and interpret the structural characteristics and features of the boundary layer. Sample results of the vorticity vector are consistent with the presence of hairpin-shaped vortices inclined downstream along the streamwise direction. These vortices envelop low speed zones and generate Reynolds shear stress that enhances turbulence production. Computation of inclination angles of individual eddy cores using the vorticity vector suggests that the most probable inclination angle is 35° to the streamwise-spanwise plane with a resulting projected eddy inclination of 43° in the streamwise-wall-normal plane.

1 Introduction

Over the past few decades, researchers have worked toward understanding the eddy structure within turbulent boundary layers in order to develop effective simplifying models. Adrian et al. (2000b) have reinforced the viewpoint that "hairpin vortices" are a primary feature in turbulence transport and production. The authors performed PIV experiments in streamwise-wall-normal planes of a turbulent boundary layer and found signatures of heads of hairpin vortices. Most significantly, they also observed that these vortices traveled together in groups, termed "hairpin packets". Recently, Ganapathisubramani et al. (2003), with stereoscopic PIV data in streamwise-spanwise planes in the logarithmic region of a turbulent boundary layer ($z^+ = 92$ and 150, where z^+ is the wall-normal location non-dimensionalized by U_τ-skin friction velocity and v-kinematic viscosity), concluded that these hairpin packets occupy only a small percentage of the total area, but contribute to a significant proportion of the total Reynolds shear stress generated, conservatively more than 30%. Hence, the hairpin packets are a very important mechanism in turbulence production. However, a detailed understanding of the three dimensional structure of hairpin vortices and packets is not yet available, and many questions remain unanswered regarding the shape, size, orientation and dynamics or these structures. To resolve the strength and orientation of a vortex, it is necessary to measure all three components of vorticity. Various analytical methods have relied on the complete velocity gradient tensor to isolate individual vortex cores (see Zhou et al. 1999; Jeong and Hussain 1995), and Chong et al. (1990) have shown that a complete description of the local flow topology can be obtained from the velocity gradient tensor.

Several researchers have used multiple hot-wire probes to measure multiple components of the gradient tensor simultaneously including the nine sensor vorticity probe developed by Balint et al. (1991). Similar 'point' gradient measurements have been made using Laser Doppler Anemometry (LDA)(see e.g. Ötügeny et al. 1998). However, the hot-wire and LDA gradient measurements are typically limited to a point

B. Ganapathisubramani · E. K. Longmire (✉) · I. Marusic
Department of Aerospace Engineering and Mechanics,
University of Minnesota, 107 Akerman Hall, 110 Union Street SE,
Minneapolis, MN, 55455
E-mail: ellen@aem.umn.edu

S. Pothos
TSI Incorporated, 500 Cardigan Road, Shoreview, MN, 55126

in space, and Taylor's hypothesis must be applied to make inferences about spatial flow structures. Standard PIV has been used in various studies to obtain four in-plane components of the velocity gradient tensor over a plane instantaneously. This enables calculation of one vorticity component (out-of-plane vorticity) over a planar field. Stereoscopic PIV and scanning PIV give the out-of-plane velocity component, and hence two more components of the velocity gradient tensor can be determined. However, the in-plane components of the vorticity vector remain unresolved with this method.

Holographic particle image velocimetry (HPIV) can provide the complete velocity gradient tensor over a volume (Meng and Hussain 1995; Zhang et al. 1997). The in-line and off-axis holographic PIV techniques (for example, see Scherer and Bernal 1997; Barnhart et al. 1994) are capable of providing a 3-D velocity field over a volume. Any velocity gradient can then be determined by differentiation. Another method capable of determining the complete gradient tensor is dual-plane stereoscopic PIV (DSPIV). This technique, which enables measurement of the complete velocity gradient tensor over a plane, has been employed previously by a limited number of research groups for various purposes. Kähler (2004) used a polarization-based dual-plane technique to compute correlations between planes with various separations in a turbulent boundary layer. Two independent stereo PIV systems measured three velocity components in two parallel planes, with the two pairs of light sheets having orthogonal polarization. The property of polarization of scattered light was used to image light from the two sheet pairs onto two independent camera pairs. The working principle of this method was based on the concept that light scattered by small particles (diameter < 10 μm) possesses the same polarization properties as the incident light. Polarization filters were placed in front of the camera lenses to allow passage of light with specific polarization. Hu et al. (2001) used the same technique to investigate large-scale features in a lobed jet. Mullin and Dahm (2005) employed a frequency-based DSPIV technique to measure the velocity gradient tensor in a turbulent shear flow. Their technique is similar to the above in principle, except that two independent stereo PIV systems measured velocity components in differentially-spaced planes illuminated by pairs of 532 nm and 635 nm laser light sheets. This method thus relied on color filters on the camera lenses to isolate one plane from another.

In the present study, a three-camera polarization-based dual-plane technique is used to measure the full velocity gradient tensor. The continuity equation is employed in combination with the PIV data to determine the appropriate quantities. The overall objective of this study is to use the three dimensional velocity gradient data to study the geometric structure and organization of vortices in the boundary layer and their relation to turbulence production.

2 Experiment and methods

Experiments were performed in a suction-type boundary layer wind tunnel. Measurement planes were located 3.3 m downstream of a trip wire in a zero-pressure-gradient flow with freestream velocity $U_\infty = 5.9$ m s^{-1} and $Re_\tau = 1160$ ($Re_\tau = \delta U_\tau / \gamma$), where δ is the boundary layer thickness). The Reynolds number based on the momentum thickness Re_θ was 2600, and the value of δ in the region of the measurement planes was 70 mm. The streamwise, spanwise and wall-normal directions are along the x, y and z axes respectively and the fluctuating velocity components along those three directions are represented as u, v and w. All quantities are normalized using U_τ and v and are denoted with a superscript $+$.

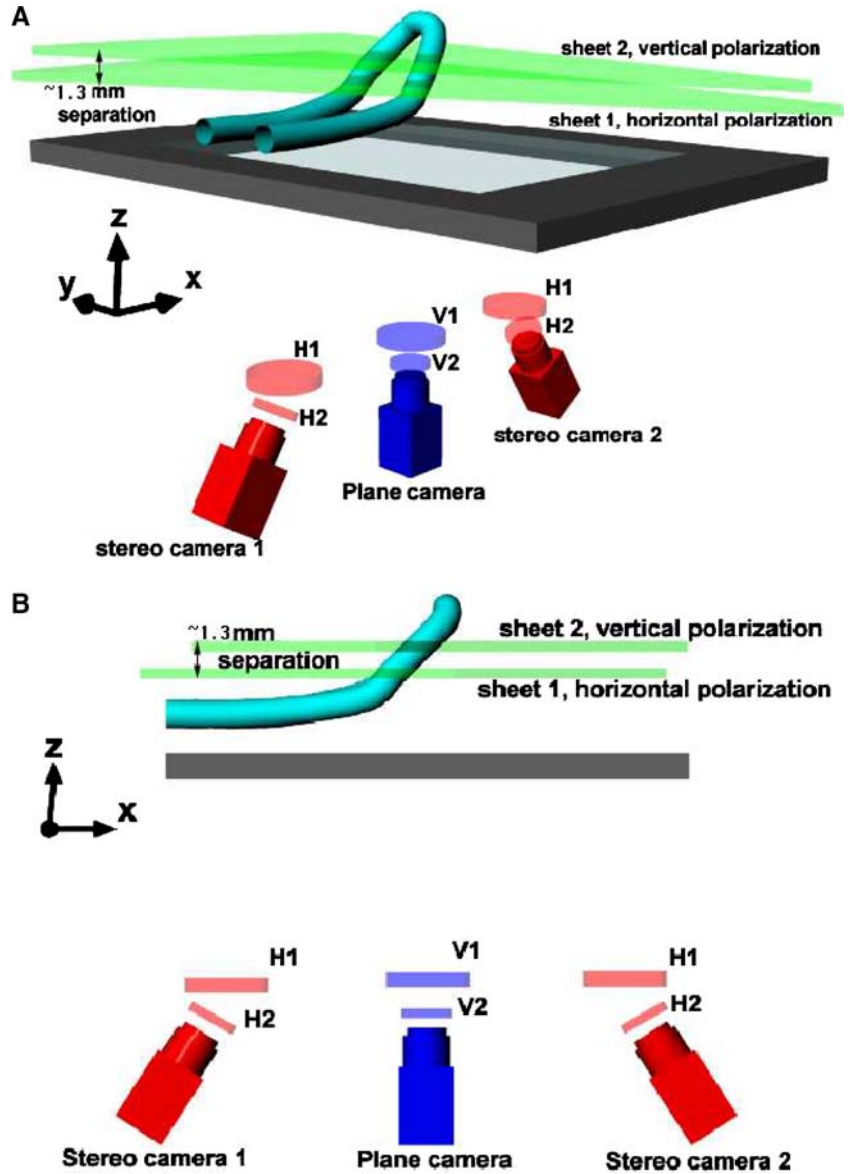The flow was seeded with olive oil droplets (size ~ 1 μm) that were generated by eight Laskin nozzle units set up in parallel. The oil droplets were ingested into the intake of the wind tunnel upstream of honeycomb straighteners and screens used for flow conditioning. At the test section, glass side-walls and a glass bottom wall were installed in the wind tunnel to provide high-quality optical access.

Two independent PIV systems capture data simultaneously in neighboring streamwise spanwise planes separated by ~ 1.3 mm (21 wall units or 22η, where η is the Kolmogorov length scale and $\eta^+ \sim 0.95$) as shown in Fig. 1. System 1, which is stereoscopic, provides three velocity components over a plane illuminated by Sheet 1, and System 2 uses a single camera to measure the streamwise-spanwise velocity components in the higher plane illuminated by Sheet 2. Simultaneous measurements are performed utilizing the polarization property of the laser light sheets to isolate one plane to one camera set. (see e.g. Kähler and Kompenhans 2000; Hu et al. 2001; Christensen and Adrian 2002).

System 1 includes two Kodak Megaplus $1k \times 1k$ pixel resolution cameras equipped with Nikon 105 mm lenses. The lenses are fitted with linear polarizers (two in series) oriented to allow the passage of horizontally-polarized light only. System 2 includes one TSI Powerview camera with $2k \times 2k$ pixel resolution and a Nikon 50 mm lens. The linear polarizers in this case are oriented to allow the passage of vertically-polarized light only. Light sheets are generated from a pair of Spectra-Physics PIV-400 series Nd:YAG laser beams (350 mJ/pulse) that are horizontally polarized. The original beams pass through a 50-50 beamsplitter (CVI-laser) as shown in Fig. 2. Half of the original energy (that is horizontally polarized) is used to illuminate the planes for system 1. The other half passes through a half-wave plate (CVI laser) to rotate the polarization by 90° and is used to illuminate the planes for system 2. Each laser-sheet pair is aligned independently to illuminate a specific wall-normal location.

The thickness of the laser sheets and the separation between the sheets of systems 1 and 2 were determined by performing burn tests at multiple spanwise locations.

A piece of laser alignment paper was placed in the measurement region, and the laser sheets exposed it leaving permanent marks on the paper. The paper was then scanned into a TIFF image with a high-quality scanner. The sheet thickness and separation values are then obtained by analyzing the TIFF image. The thicknesses of the laser sheets for Systems 1 and 2 were found to be 0.35 and 0.45 mm respectively based on the full width of the burn mark left on the paper.

Although the burn method is not the most accurate technique for determination of sheet thickness (depending on the laser power and beam profile, this method could either under or overestimate the sheet thickness), it is sufficiently accurate to determine the sheet separation. The separation between the centerlines of the burn marks of each sheet was found to be 1.3 mm. The uncertainty in measuring the separation between the sheets was estimated to be 0.1 mm based on the TIFF scans and is independent of the uncertainty associated with sheet thickness. The measurement of sheet separa-tion(critical to the determination of $\partial U/\partial z$ and $\partial V/\partial z$) with a more accurate method is a goal for our future work using the present technique.

Vector fields for the $1k \times 1k$ cameras were computed using the adaptive central-difference technique outlined
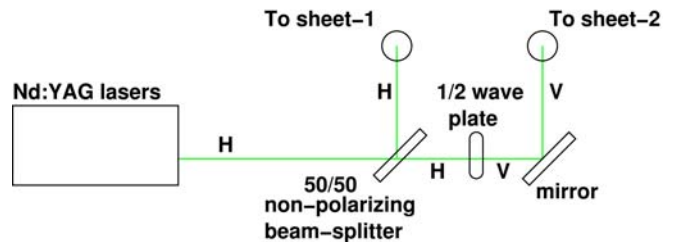

Fig. 2 Top view of laser setup. V and H designate the direction of vertical and horizontal polarization respectively

in Wereley and Meinhart (2001) using TSI *Insight 6.1* with a final window size of 16×16 pixels (no smoothing was applied). The final interrogation windows had 50% overlap. The vectors from each camera in the stereo plane were then combined using suitable magnification factors to compute all three velocity components (see Ganapathisubramani et al. 2002 for details). In order to maintain a similar spatial resolution as in the stereoscopic plane, the vector fields from the Powerview camera were computed using 32×32 pixel windows with 50% overlap(final size) using the same central difference technique. The resulting vector fields from the single camera were resampled and mapped onto the grid of the stereo measurement using inverse-distance interpolation. The resolution of the resulting vector fields was about 14 × 14 wall units ($15\eta \times 15\eta$), and the total field size was $1.1\delta \times 1.1\delta$.

The average pixel displacements in the stereo plane and the single camera plane were 6 and 15 pixels respectively. The vector fields were validated using a standard Gaussian engine that removed vectors with values outside of 4 standard deviations from the mean. Any missing vectors were interpolated using a 3×3 local mean technique. The number of spurious vectors was close to 4% in the stereo plane and less than 3% in the single camera plane.

The single camera vector field from the upper plane in liaison with the stereoscopic data from the lower plane was used to compute all velocity gradients in the lower plane. A second-order central-difference method was used to compute all possible in-plane gradients while a first-order forward-difference was used to compute the wall-normal gradients of the streamwise and spanwise velocities. Finally, the continuity equation was used to recover the wall-normal gradient of the wall-normal velocity.

2.1 Uncertainty in computed gradients

An uncertainty analysis was performed to quantify the accuracy of the computed gradients. The uncertainty in any computed velocity gradient is dependent on the uncertainty in the velocity component measured, in the separation between points and in the differencing scheme used to compute the gradient (see Raffel et al. 1998). A simple error propagation analysis was employed to compute the uncertainties in the gradients at a single point as described by Kline and McClintock (1953). Table 1 lists the computed absolute uncertainty in all 9 gradients and values normalized by each r.m.s (root mean square) of the gradients.

For in-plane velocity gradients, the primary contributions to the uncertainty come from the pixel resolution and stereoscopic reconstruction. The uncertainty in sheet separation makes a significant contribution to the uncertainty in the gradient in the wall-normal direction for $\partial U/\partial z$ and $\partial V/\partial z$. Considering all nine gradients, the largest absolute uncertainties occur for $\partial W/\partial x$ and

Table 1 Uncertainties in velocity gradients at $z^+ = 110$. K is any gradient, σ_K is the r.m.s of K, δK is the uncertainty in the gradient with value σ_K

K	σ_K (s^{-1})	δK (s^{-1})	% $\delta K/\sigma_K$
$\partial U/\partial x$	104	14.6	14
$\partial U/\partial y$	165	14.6	9
$\partial U/\partial z$	192	23.6	12
$\partial V/\partial x$	123	26.2	21
$\partial V/\partial y$	115	26.2	22
$\partial V/\partial z$	182	29.2	16
$\partial W/\partial x$	167	74.8	44
$\partial W/\partial y$	188	74.8	39
$\partial W/\partial z$	123	30.2	24

$\partial W/\partial y$. These large values are dominated by uncertainty in the stereoscopic reconstruction algorithm. The absolute uncertainty in the gradients $\partial U/\partial z$ and $\partial V/\partial z$ increases with uncertainty in sheet separation so that these values are typically larger than those for the corresponding in-plane gradients. The column denoted by δK shows the absolute uncertainty in a measurement equal to the r.m.s. value for each gradient. Note that in the experimental dataset discussed below, the values of gradients used to identify vortex cores are typically at least twice the r.m.s. value. As a result, the relative uncertainty in the gradients of interest to this study is smaller than values reported in column 4 by a factor of two or more. The following paragraph illustrates this important point by citing examples of typical values of vorticity components (computed using these gradients) and the uncertainty associated with them.

Consider a relatively weak vortex core (weak in magnitude from the swirl strength values) located at (x^+, y^+) of $(0,-200)$ in Figs. 5a, b. The wall-normal vorticity ($\omega_z = \partial V/\partial x - \partial U/\partial y$) at a point in this core has a value of -275 s^{-1} (r.m.s value of ω_z is 240 s^{-1}). The uncertainty in this value of ω_z based on the values indicated in Table 1 is 11%. The streamwise-vorticity component ($\omega_x = \partial W/\partial y - \partial V/\partial z$) at the same point has a value of 624 s^{-1} (the r.m.s value ω_x is 270 s^{-1}). The uncertainty in the value of ω_x using the values indicated in Table 1 is 12%. Similarly, a typical value for spanwise vorticity ($\omega_y = \partial U/\partial z - \partial W/\partial x$) at a point in a relatively weak spanwise oriented vortex core is 480 s^{-1} (r.m.s value of ω_y is 250 s^{-1}). The uncertainty in this value of ω_y based on the values in Table 1 is 16%. The above examples reflect the findings of Westerweel (1994), where the author computed the uncertainty in vorticity in a one dimensional shear layer using synthetic PIV images. This study revealed that the value of vorticity could be computed with 10–20% accuracy at best (depending on the measurement noise), provided the velocity data are within 1–2% accuracy.

It should be noted that the uncertainty in the wall-normal gradients cannot be improved much further by using a four-camera dual-plane stereoscopic PIV technique. Accuracy of wall-normal gradients depends primarily on accuracy of the velocity component and determination of sheet separation. Therefore, three-

component velocity field information in two differentially-separated planes is redundant. However it can be used to validate the technique by comparing the computed gradients against continuity (see Mullin and Dahm 2005).

The validity of the dual-plane gradients in the present study can be judged further by computing the wall-normal gradient of mean streamwise velocity ($\partial \bar{U}/\partial z$). This value can be compared with the wall-normal gradient predicted by the log law:

$$\frac{\partial \bar{U}}{\partial z} = \frac{U_\tau}{\kappa z},$$

where z is the wall normal location and $\kappa = 0.41$ is the universal log-law constant. For our wall-normal location, which is 6.7 mm from the wall, and skin friction velocity $U_\tau = 0.25$ m s^{-1}, the log law predicts the gradient to be 90.34 s^{-1}. The measured average value from an ensemble of 1200 images (with resolution of 100×100 vectors) is 87.82 s^{-1}. The error in the mean value of the gradient is thus 2.8% which is well within the expected uncertainty for this first order difference quantity.

The r.m.s statistics of the three vorticity components were computed, and they compare well with previous data in the literature. The r.m.s values of all three vorticity components measured in this experiment are within 5–10% of the corresponding values measured using hot-wires by Balint et al. (1987) ($Re_\theta = 2080$), Balint et al. 1991 ($Re_\theta = 2685$) and Honkan and Andreopoulos (1997) ($Re_\theta = 2790$) and computed by Spalart (1988) in a direct numerical simulation(DNS) ($Re_\theta = 1410$). The differences in the r.m.s. values are well within the uncertainty limits of the measurements. Since, the gradients computed in this study are used to examine coherent vortex structures, as opposed to the details of small scale turbulence, the agreeable comparison of our data with the previous literature suggests that the mea-

surement technique is acceptable for the application chosen.

3 Results and discussion

In all vector plots presented, the flow is from left to right, and the local mean $\bar{U}$ is subtracted from the vectors to clearly illustrate the slow and fast moving zones. The contour and vector plots shown in all figures are computed from a single realization, but the patterns are representative of those found in many vector fields.

Figure 3a, b show the streamwise velocity fluctuation (u^+) contours from the lower ($z^+ = 110$) and upper planes ($z^+ = 130$) respectively. It is clear that the two planes are very well correlated. The streamwise velocity signature consists of narrow and elongated low- and high-speed regions. The region marked with a box in the figure contains a signature of a "hairpin packet" as identified by the feature extraction algorithm described in Ganapathisubramani et al. (2003). The algorithm first searched for regions of strong positive wall-normal vorticity (ω_z) lying above regions of strong negative vorticity. Between the positive and negative vorticity regions, it identified points of strong instantaneous Reynolds shear stress ($-uw$), that served as seed points for a region growing algorithm. All interconnected points with similar streamwise velocity were then included in the packet region. In subsequent plots, we present a zoomed in view of the boxed area in order to focus on the details of the packet region.

The wall-normal (ω_z^+) and streamwise (ω_x^+) components of vorticity of the boxed region are plotted in Fig. 4a, b. As seen from Fig. 3, this region is centered on a low-speed zone. The plot of ω_z^+ shows that the low-speed region is enveloped by negative values on the top and the positive values on the bottom. Also, the vectors seem to indicate that these regions of vorticity contain swirling motions indicative of vortex cores. However, the vortices seen here are not merely wall-normal vor-

Fig. 3 Fluctuating streamwise velocity (u^+) contours at (**a**) $z^+ = 110$; $\bar{U}_1^+ = 16.04$, (**b**) $z^+ = 130$; $\bar{U}_2^+ = 16.48$
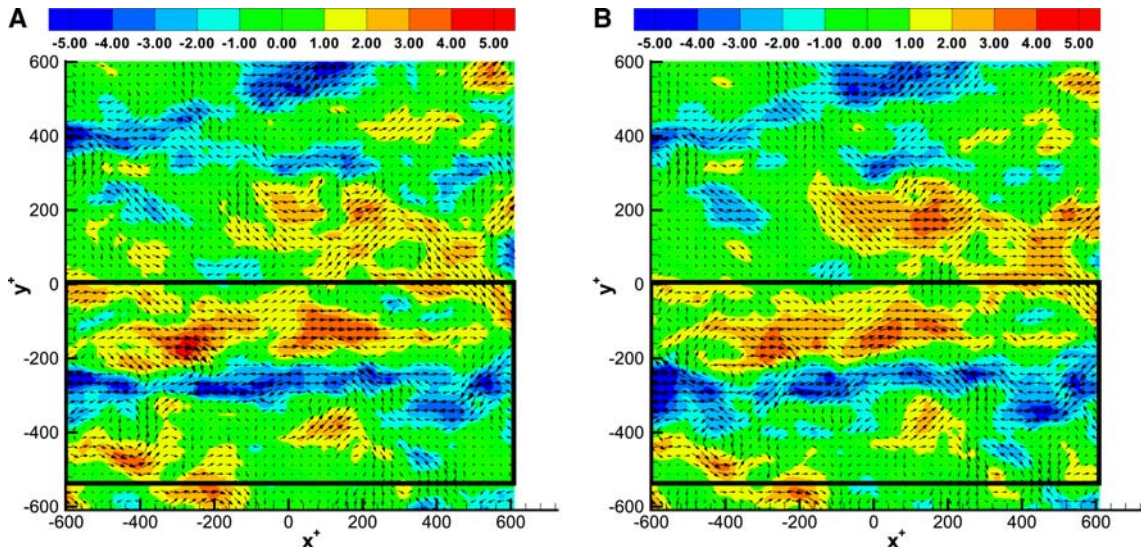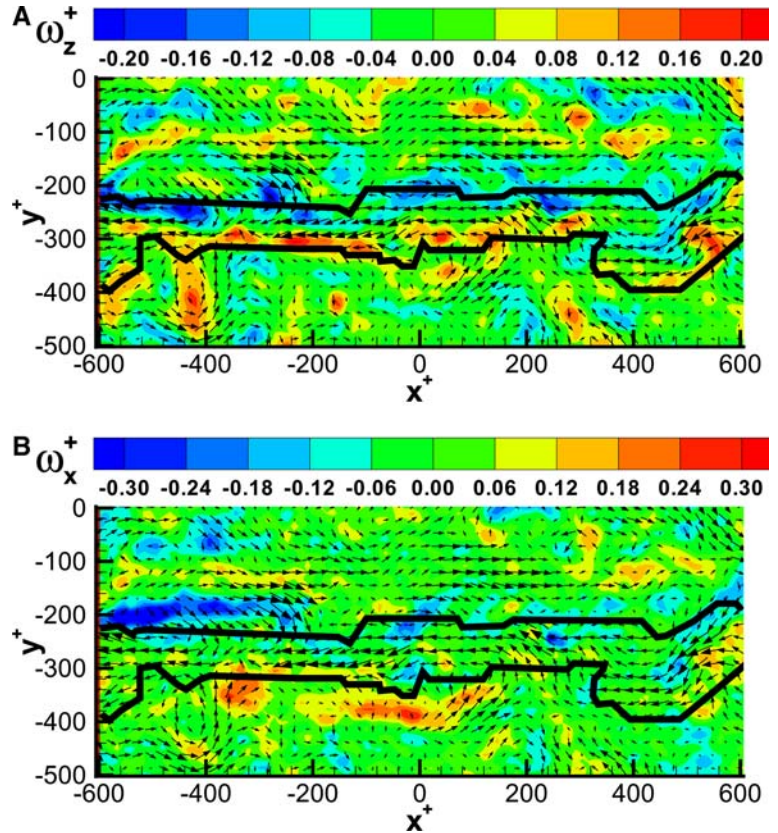
Fig. 4 Various quantities at $z^+ = 110$ (**a**) ω_z^+, (**b**) ω_x^+. The dark line in the plots is the envelope of a low-speed region identified as a hairpin packet by the algorithm described in Ganapathisubramani et al. (2003)


tices. This point becomes clear from the ω_x^+ plot. The regions of positive ω_z^+ have predominantly positive ω_x^+, and regions of negative ω_z^+ have negative ω_x^+. The data thus suggest the presence of vortices inclined at an angle with respect to the streamwise direction which would be expected from a cross sectional view of a series of hairpin-type vortices. Note, however, that inclined hairpin-type signatures are not the only type of instantaneous structures observed. Examination of various vector fields in the two neighboring planes indicates evidence of some structures that are inclined at 90 degrees to the streamwise direction and others that are completely streamwise.

To present more concrete evidence that regions of strong vorticity correspond with vortex cores, we examine plots of the instantaneous swirl strength for the same 'boxed' region shown in Fig. 3. Various analytical methods have relied on the complete velocity gradient tensor to isolate individual vortex cores. Chong et al. (1990) Dallmann (1983) and Jeong and Hussain (1995) among others have shown that a complete description of the local flow topology can be obtained from the velocity gradient tensor. In this study, swirl strength (λ_{3D}), which is the imaginary part of the complex eigenvalue of the velocity gradient tensor (see Zhou et al. 1999), is used. This quantity isolates regions where fluid swirls about an axis in the flow field. Two-dimensional swirl strength(λ_{2D}) can be computed using the gradient tensor that contains only the in-plane velocity gradients (Adrian et al. 2000a).

Values of swirl strength are computed from the velocity gradients obtained from the PIV datasets. We note that uncertainties in the individual velocity gradients must lead to uncertainties in the values of computed swirl strength. A direct quantification of this uncertainty is not possible given the interdependence of the various gradients within coherent structures. However, unlike vorticity, finite values of swirl strength require the presence of multiple gradients with significant strength and appropriate sign (vorticity requires only one strong gradient). This requirement will act toward suppressing the effect of random noise on false positive identification of vortex cores. Also, our results show that significant swirl strength tends to occur in groups of contiguous points, rather than at a single point, suggesting that swirl is a good qualitative identifier of vortex cores as opposed to an identifier of noise.

Figure 5a reveals the instantaneous two dimensional swirl strength (λ_{2D}^+) at $z^+ = 110$. (Note that in Figure 5, only every second vector is plotted). This plot in tandem with ω_z^+ (see Fig. 4a) shows that 2-D swirl isolates regions that are swirling about an axis aligned with the wall-normal direction. A visual comparison between the locations of swirl in the lower and upper planes (not shown here) indicates a forward tilt to most structures as they are offset in the positive streamwise direction in the upper plane. (This trend is observable in many pairs of planes, in particular when they are viewed in rapid succession). However, if the inclination of vortices with respect to the wall is small, λ_{2D}^+ does a poor

Fig. 5 Various quantities at $z^+ = 110$ (**a**) λ^+_{2D} and (**b**) λ^+_{3D}. The dark line in the plots is the envelope of a low speed region identified as a hairpin packet by the algorithm described in Ganapathisubramani et al. (2003)
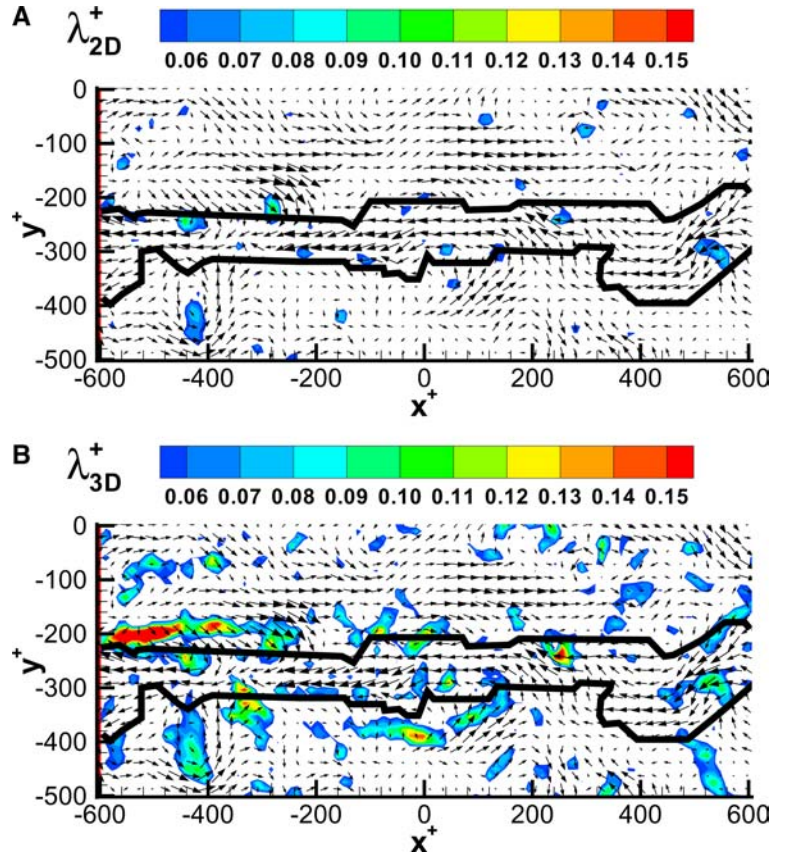
job at identifying them. Figure 5b presents a plot of the full swirl strength (λ_{3D}^+) computed utilizing the complete velocity gradient tensor. The plot reveals that the 3-D swirl identifies not only the hairpin-shaped vortices cutting across the plane but also additional regions not isolated by 2-D (wall-normal) swirl. The magnitudes of λ_{3D}^+ are typically larger than λ_{2D}^+ in the same location suggesting some deviation from the wall-normal direction. Note for example, the location at the downstream end of the packet that contains elongated regions of significant λ_{3D}^+ but not λ_{2D}^+. It could be speculated that these regions could possibly coincide with angled necks of a hairpin vortex that are cutting across the measurement volume with a shallow angle and hence are not completely apparent in the 2-D swirl plot.

Figure 6 reveals additional information about the same "hairpin packet". Figure 6a, b show contours of u^+ and uw^+. These plots demonstrate that the hairpin packet is a low-speed zone which contains significant Reynolds shear stress in multiple spatially compact regions. Figure 6c shows instantaneous production, defined as $uw^+(\partial U^+/\partial z^+)$[1]. Some locations of strong

production lie close to swirling zones. Figure 6c shows high production levels in the packets near the legs of hairpins (for example, the middle of the packet at $x^+ = 0$ has high production zones on either side of a swirl). Other examples (not shown here) reveal strong Reynolds stress production in regions that lie close to zones of significant λ_{3D}^+ (but, not λ_{2D}^+) that could be spanwise heads or streamwise oriented legs of hairpin vortices, and these sites can be considered as alternate zones for turbulence production.

The dual-plane data can also be used to compute the inclination angle of vortices by determining the orientation of the vorticity vector averaged over the region of a vortex core. It is important to distinguish this quantity from an instantaneous vorticity vector angle at a point. In that case, the dominant signal may be from small-scale fluctuations. By contrast, computation of the vorticity vector averaged over a core region identified by the swirl strength λ_{3D}^+ filters out small-scale incoherent contributions and leads to determination of the core orientation. This orientation can then be interpreted as the local inclination of that vortex.

Figure 7 reveals the probability density function (p.d.f.) of the inclination angle (θ_e) that vortex cores make with the $x-y$ plane. The angles were computed for all distinct regions of significant λ_{3D}^+ ($\lambda_{3D}^+ >$ **th**, **th** $= 0.1\lambda_{3D\text{-max}}^+$, where $\lambda_{3D\text{-max}}^+$ is the maximum 3-D swirl strength value in the dataset). Additional criteria (detailed in Ganapathisubramani 2004) were employed to

---

[1]This is consistent with Brodkey et al. (1973) who provided an interpretation of production, based on instantaneous Reynolds shear stress and instantaneous wall-normal gradient, where the production term almost exactly balances dissipation. Other definitions have also been proposed (see Bradshaw 1974).

Fig. 6 Various quantities at z^+ = 110. (a) u^+, (b) uw^+, (c) Instantaneous production, $uw^+((\partial U^+)/(\partial z^+))$. The dark line in the plots is the envelope of a low-speed region identified as a hairpin packet by the algorithm described in Ganapathisubramani et al. (2003)
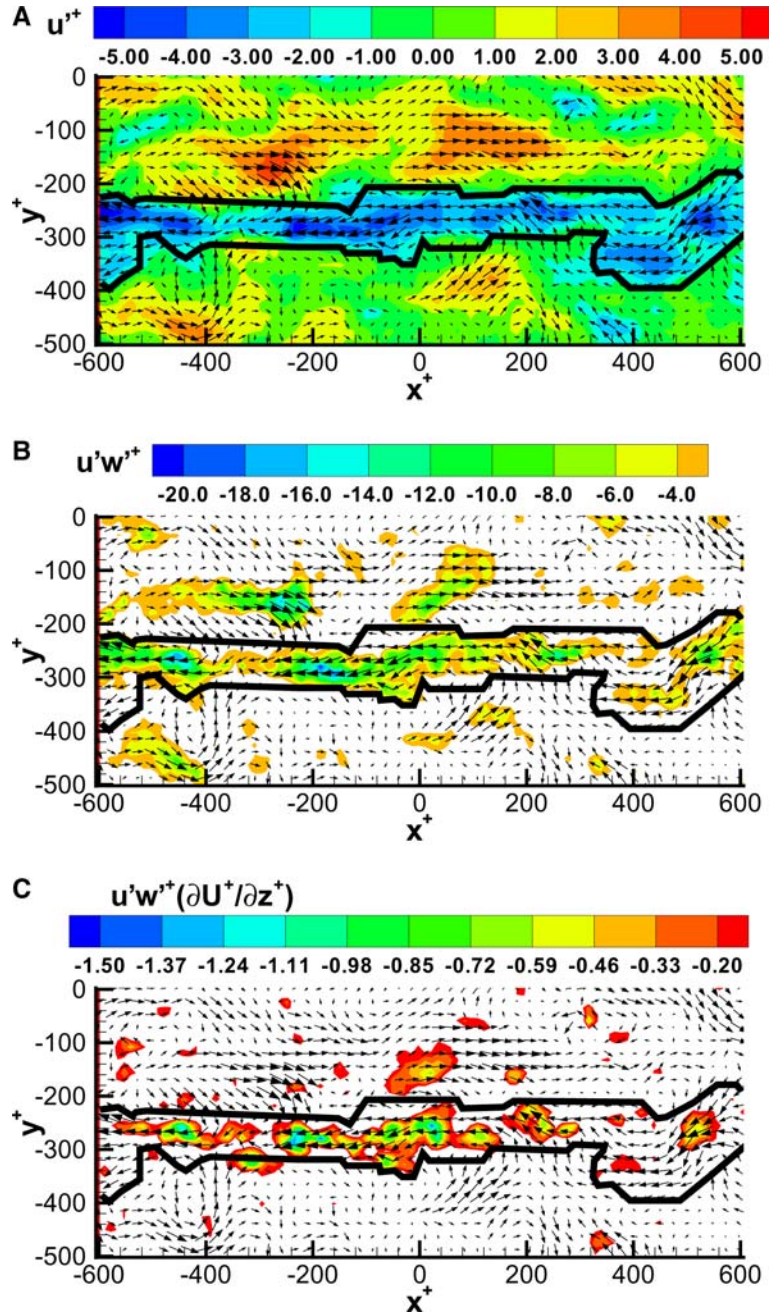
minimize any effect of high frequency noise on the distribution due to the use of gradient data. Each core was required to contain a minimum of 5 contiguous points. Also, the average enstrophy (square of the vorticity magnitude) for any core was required to be greater than 10% of the maximum enstrophy measured in the dataset. These thresholds were chosen to isolate a significant number of cores for statistical convergence while minimizing the influence of measurement noise on the results.

The resulting distribution (closed squares) includes a wide range of core inclination angles at this wall-normal location. Note that many cores have small inclination angles. Further investigation of the probability distribution of the azimuthal angle of these cores (θ_{xy}, angle made by the projection of the vorticity vector onto the $x-y$ plane with the x axis) indicates two peaks. One consistent with the presence of spanwise heads (θ_{xy} = 90°) and the other with streamwise-oriented legs (θ_{xy} = 0°). In order to obtain the inclination angles of cores that are not aligned parallel with the measurement plane, the average vorticity vector was computed in isolated regions of λ_{3D}^+ that include λ_{2D}^+ ($\lambda_{2D}^+ > 0$). This additional criterion filters out spanwise and streamwise structures. The resulting p.d.f. (open circles in figure Fig. 7) yields peaks at ±35°. This suggests that most cores are inclined at 35° to the $x-y$ plane. Note, however, that the peaks are broad, and a wide range of inclination angles is still present. The angle made by the
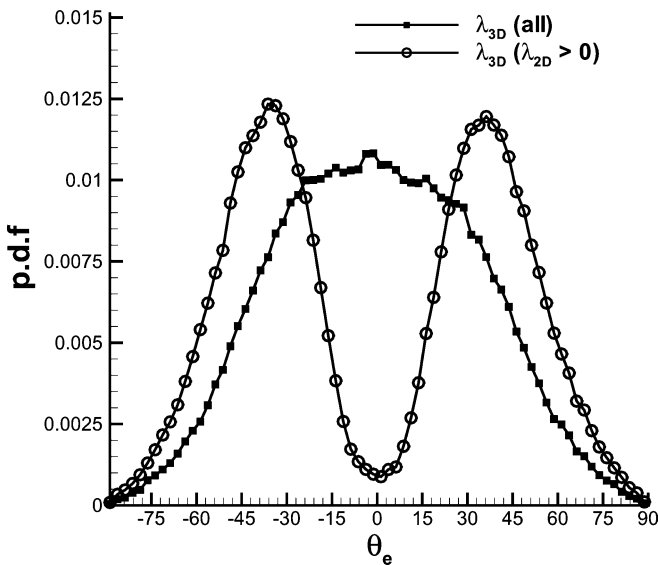
Fig. 7 p.d.f. of inclination angle (θ_e)

projection of the core vorticity vector in the $x-z$ plane with the x axis is defined as the eddy inclination (θ_i). The most probable eddy inclination angle was found to be 43°. This is comparable to a 45° inclination of hairpin-type vortices as suggested by various researchers over the past century (Head and Bandyopadhyay 1981).

4 Conclusions

Simultaneous dual-plane PIV experiments were performed to compute all nine velocity gradients in a turbulent boundary layer. The technique employed a three-camera system where one plane of data was obtained with a stereoscopic camera pair and the second plane with a single camera. Orthogonal polarization of the two light sheets was used to separate the light scattered by tracer particles onto the appropriate cameras. The out-of-plane gradient of the out-of-plane velocity component was obtained by continuity. The maximum uncertainty in gradient measurements occurs in $\partial W/\partial x$ and $\partial W/\partial y$ due to the uncertainty in W caused by reconstruction of stereo PIV. The relatively smaller uncertainty in the out-of-plane gradients of U and V could be reduced by improving the accuracy in determining the separation between laser sheets.

The measurements were used to compute the complete vorticity vector and other quantities like instantaneous Reynolds shear stress production and 3-D swirl strength to study the eddy structure. The mean and r.m.s statistics of the vorticity components compare well with the data available in the literature and the computed wall-normal gradient of the streamwise velocity component is in agreement with the value predicted by the logarithmic law of the wall.

Contours of different vorticity components and 2-D swirl strength from the two neighboring planes indicate

the existence of groups of vortices inclined downstream along the streamwise direction consistent with the presence of hairpin vortex packets. These vortices envelop low speed zones and generate patches of Reynolds shear stress that enhance turbulence production. Plots of 3-D swirl strength indicate the existence of additional vortex cores within the low speed zones that may represent heads of smaller eddies intersecting the measurement plane.

The dual-plane data was also used to calculate the distribution of vortex inclination angles at this wall-normal location. The most probable inclination angle (θ_e) with the streamwise-spanwise plane was found to be $\pm 35°$. This gives an eddy inclination angle (θ_i, as projected onto the streamwise-wall-normal plane) of 43°. This value compares favorably with other studies that indicated that average hairpin vortices are inclined at 45° with the streamwise direction. However, it is worth noting that this study includes data at only one wall-normal location, and datasets at multiple wall-normal locations would be required to resolve the complete vortex structure. This can be accomplished easily in the future using the present measurement technique.

References

Adrian RJ, Christensen KT, Liu ZC (2000a) Analysis and interpretation of instantaneous turbulent velocity fields. Exp Fluids 29:275–290

Adrian RJ, Meinhart CD, Tomkins CD (2000b) Vortex organization in the outer region of the turbulent boundary layer. J Fluid Mech 422:1–53

Balint J-L, Wallace JM, Vukoslavcevic P (1987) A study of vortical structure of the turbulent boundary layer. In: Comte-Bellot G, Mathieu J (eds) Advances in Turbulence. Springer, Berlin Heidelberg New York, pp 456–464

Balint J-L, Wallace JM, Vukoslavcevic P (1991) The velocity and vorticity vector fields of a turbulent boundary layer. Part 2. Statistical properties. J Fluid Mech 228:53–86

Barnhart DH, Adrian RJ, Meinhart CD, Papen GC (1994) Phase-conjugate holographic system for high resolution particle image velocimetry. Appl Opt 33:7159–7169

Bradshaw P (1974) Comments on turbulent energy production, dissipation and transfer. Phys Fluids 17(11):2149

Brodkey RS, Nychas SG, Taraba JL, Wallace JM (1973) Turbulent energy production, dissipation and transfer. Phys Fluids 16(11):2010–2011

Chong MS, Perry AE, Cantwell BJ (1990) A general classification of three-dimensional flow fields. Phys Fluids A 2(5):765–777

Christensen KT, Adrian RJ (2002) Measurement of instantaneous Eulerian acceleration fields by particle image accelerometry: method and accuracy. Exp Fluids 33:759–769

Dallmann U (1983) Topological structures of three-dimensional flow separations. In: DFVLR Report No. IB 221-82-A07, Göttingen, Germany

Ganapathisubramani B (2004) Investigation of turbulent boundary layer structure using stereoscopic particle image velocimetry. Ph.D. thesis, University of Minnesota, USA

Ganapathisubramani B, Longmire EK, Marusic I (2002) Investigation of three dimensionality in the near field of a round jet using stereo PIV. J Turbulence 3:17

Ganapathisubramani B, Longmire EK, Marusic I (2003) Characteristics of vortex packets in turbulent boundary layers. J Fluid Mech 478:35–46

Head MR, Bandyopadhyay P (1981) New aspects of turbulent boundary-layer structure. J Fluid Mech 107:297–337

Honkan A, Andreopoulos Y (1997) Vorticity, strain-rate and dissiipation characteristics in the near-wall region of turbulent boundary layers. J Fluid Mech 350:29–96

Hu H, Saga T, Kobayashi T, Taniguchi N, Yasuki M (2001) Dual-plane stereoscopic particle image velocimetry: system set-up and its application on a lobed jet mixing flow. Exp Fluids 31:277–293

Jeong J, Hussain F (1995) On the identification of a vortex. J Fluid Mech 258:69–94

Kähler CJ (2004) Investigation of the spatio-temporal flow structure in the buffer region of a turbulent boundary layer by means of multiple plane stereo PIV. Exp Fluids 36:114–130

Kähler CJ, Kompenhans J (2000) Fundamentals of multiple plane stereo particle image velocimetry. Exp Fluids (Suppl):S70–S77

Kline SJ, McClintock FA (1953) Describing uncertainties in single-sample experiments. Mechanical Engineering 75:3–8

Meng H, Hussain F (1995) Instantaneous flow field in an unstable vortex ring measured by HPIV. Phys Fluids 7:9–11

Mullin JA, Dahm WJA (2005) Dual-plane stereo particle image velocimetry (DSPIV) for measuring velocity gradient fields at intermediate and small scales of turbulent flows. Exp Fluids 38:185–196

Ötügeny MV, Su W, and Papadopoulosz G (1998) A new laser-based method for strain rate and vorticity measurements. Meas Sci Technol 9:267–274

Raffel M, Willert C, Kompenhans J (1998) Particle image velocimetry - A practical guide. Springer, Berlin Heidelberg New York

Scherer JO, Bernal LP (1997) In-line holographic particle image velocimetry for turbulent flows. Appl Opt 36:9309–9318

Spalart PR (1988) Direct simulation of turbulent boundary layer up to $Re_{\theta=1410}$. J Fluid Mech 187:61–98

Wereley ST, Meinhart CD (2001) Second-order accurate particle image velocimetry. Exp Fluids 31:258–268

Westerweel J (1994) Digital Particle Image Velocimetry - Theory and Applications. Delft University Press

Zhang J, Tao B, Katz J (1997) Turbulent flow measurement in a square duct with hybrid holographic PIV. Exp Fluids 23:373–381

Zhou J, Adrian RJ, Balachandar S, Kendall TM (1999) Mechanisms for generating coherent packets of hairpin vortices in channel flow. J Fluid Mech 387:353–396